A study on heat affected zone softening in resistance spot welded dual phase steel by nanoindentation

Victor Hugo Baltazar Hernandez ·
Sushanta Kumar Panda · Yasuaki Okita ·
Norman Y. Zhou

Abstract The base metal (BM) and the heat affected zone (HAZ) of a resistance spot welded dual phase steel have been evaluated by nanoindentation hardness testing. Three different surface conditions have been explored on the BM for assessing the nanohardness response. Softening has been investigated along the sub-critical HAZ by making nanoindentations on individual phases such as ferrite and tempered martensite (TM) at various distances from the line of lower critical temperature Ac_1. A broken appearance accompanied with sub-micron particles were consistently found on TM at 100 μm from the Ac_1 line suggesting carbide precipitation along with partial recovery of martensite. The morphology of TM kept on changing while moving away from Ac_1 towards the BM as the fraction of broken appearance was reduced and the sub-micron particles became finer. SEM observations resulted in good agreement with the nanohardness of the TM phase along the sub-critical HAZ. In contrast, microhardness results suggested the termination of tempering at a shorter distance with respect to Ac_1 and hence a reduced extension of the softening region. The improved resolution for assessing softening through nanoindentation was due to the possibility of avoiding the contribution of the phase boundaries because of the smaller size of the indentation; this also permitted evaluation of TM at low peak temperatures far from Ac_1 where early stages of tempering took place.

Introduction

Advanced high strength steels (AHSS) offer increased ultimate strength along with good ductility making them advantageous for automotive applications. Dual phase (DP) steel is part of the family of AHSS and is composed of a ferritic matrix and varied volume fractions of dispersed martensite particles [1].

Resistance spot welding (RSW) is one of the most prevalent and preferred welding processes for joining automotive body parts. RSW of DP steel sheets has become a very important issue due to an increased number of applications on auto-body structures [2]. Measured softening (i.e. reduction in microhardness with respect to base metal (BM)) has been reported on the heat affected zone (HAZ) of resistance spot welded DP steel [3–6]. HAZ-softening has been found to be responsible for strain-localised failures due to reduction in local strength in welded DP steels leading to modified mechanical properties in laser weldments [7]. Softening has been associated with tempering of martensite in the HAZ of laser welded

V. H. Baltazar Hernandez (✉) · Y. Okita · N. Y. Zhou
Centre for Advanced Materials Joining, University of Waterloo,
200 University Ave. West, N2L3G1 Waterloo, ON, Canada
e-mail: v.h.baltazar@gmail.com; vhbaltaz@uwaterloo.ca

Y. Okita
e-mail: okita@uwaterloo.ca

N. Y. Zhou
e-mail: nzhou@uwaterloo.ca

V. H. Baltazar Hernandez
MPyM-EPMM Academic Unit of Engineering, Autonomous
University of Zacatecas, 801 Ramon Lopez Velarde Avenue,
98000 Zacatecas, Mexico

S. K. Panda
Mechanical Engineering, Indian Institute of Technology
Kharagpur, Kharagpur 721302, India
e-mail: sushanta.panda@mech.iitkgp.ernet.in

Y. Okita
JFE Steel Corporation, 1 Kawasaki-cho, Chou-ku,
Chiba 260-0835, Japan

dual phase steels [8]. Softening phenomena has also been reported in Cr steels upon higher heat input welding processes [9, 10].

Microstructure analysis from the fusion zone (FZ) through the HAZ of resistance spot welded DP steel has been little reported [11–14]. All reports agreed well that the FZ microstructure was composed of predominant martensite. Observations addressed towards the HAZ indicated that decomposition of austenite took place before re-transformation into new martensite and ferrite [11]. In order to better analyse the gradient of microstructures at the HAZ, it was conveniently divided as: *coarse grain region*; comprise blocky martensitic grains, and *intercritical region*; where martensite phase was coarsen [12]. Even though some of the above-mentioned works have reported measured HAZ-softening in resistance spot welded DP steel; no discussion has been addressed towards the tempered martensite (TM) microstructure occurring at the sub-critical HAZ.

Tempering of martensite occurs at temperature below the lower critical (Ac_1) and was also reported as the main reason for softening in martensitic steels [15, 16]. The degree or severity of tempering is highly dependent on the maximum (peak) temperature and the time at peak temperature during isothermal heat treatments, and the prior microstructure and the alloying level [17]. Martensite tempering is developed in a series of stages up to Ac_1 temperature and basically involves: the segregation of carbon, the precipitation of a transition carbide (ε-carbide), the decomposition of retained austenite, the replacement of ε-iron carbide by cementite, the coarsening of cementite or dissolution into more stable alloy carbides and the recovery of martensite [18]. Even though the tempering of martensite has been extensively investigated for martensitic steels subjected to isothermal heat treatments, little work has been addressed to investigating the process of tempering on martensite particles of DP steel during fast thermal cycles (far from equilibrium) like those generated by the RSW process.

Instrumented indentation testing (IIT) has become a valuable tool for evaluating material properties (i.e. nanohardness and elastic modulus) of small features at nano-scale [19, 20]. IIT through ball nanoindentation has been performed in order to calculate constitutive properties in welded high strength steel [21]. To date, there are few studies using IIT for assessing the degree of tempering in martensitic steels [22, 23]. Research work on analysing the nanohardness of TM particles in DP steel has been hardly reported; however, it has been shown that it is feasible to analyse the change in hardness at nano-level [24]. Thus, the present work aims to evaluate the tempering of martensite in DP steel through nanohardness measurement by IIT on a range of sub-critical HAZ microstructures developed by

rapid thermal cycles of RSW. Additionally, various surface conditions (metallographic surface preparation procedures) of the BM have been systematically investigated for assessing nanohardness of individual phases in DP steel.

Experimental

The material for the present study was a DP steel with a nominal ultimate tensile strength of 980 MPa (DP980). The DP steel was used in the form of sheet with a thickness of 1.2 mm overlaid with a galvannealed coating. The chemical composition of the bulk metal of this DP steel is provided in Table 1. The BM microstructure showing the ferrite matrix along with martensitic islands is displayed in Fig. 1. The volume fraction of martensite phase in BM was estimated to be 48% from standard metallographic and image analysis techniques.

The BM specimens were cross-sectioned along the rolling direction, mechanically ground and polished by conventional metallographic techniques. Three different surface conditions were investigated and samples were prepared according to the following procedures: (1) *mechanically fine polished*, consisted of polishing down to 0.25 μm followed by fine polishing with 0.05 μm colloidal silica; (2) *chemically etched*, consist of mechanically fine polishing followed by etching with 2% nital solution for a period of 8–10 s in order to further remove possible hardened layers; (3) *electropolished*, after grinding and

Table 1 Chemical composition for dual phase steel (wt%)

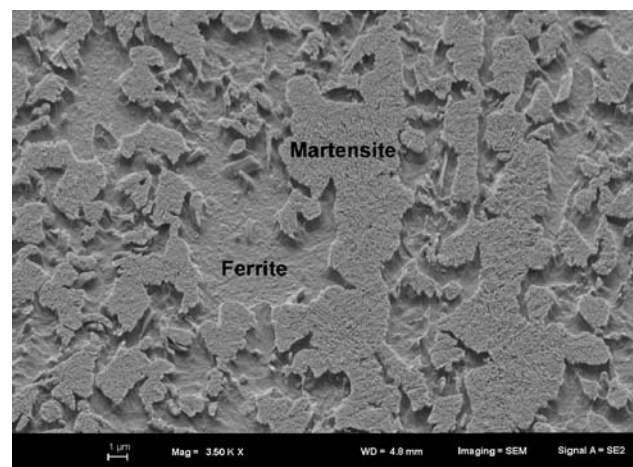| C	Mn	Si	P	S	Mo	Cr
0.13	1.91	0.03	0.01	0.005	0.33	0.16

Fig. 1 Base metal microstructure of dual phase steel under etched condition

polishing, specimens were immersed in a solution of 90% of acetic acid and 10% of $HClO_4$, a voltage of 25 V was applied for a period of 60 s. It was assumed that the electropolishing procedure fully removed any hardened layer on the surface. Roughness parameters were calculated from the topographic profiles obtained under scanning probe microscopy (SPM). Roughness was measured in selected areas of 100 μm^2 per surface condition. Roughness was also obtained for individual phases in the case of the chemically etched and the electropolished specimens. The average of the absolute value (R_a) along with the maximum height of the profile (R_t) were estimated.

The DP steel was resistance spot welded (RSW) using a conventional 60 Hz single phase alternating current (AC) resistance welding machine with air-over-hydraulic electrode loading system. The main welding parameters utilised were: 8 kA welding current, 3.5 kN electrode force and 20 cycles current duration. A pre-weld squeeze time of 25 cycles and a post-weld hold time of 5 cycles were used to complete the welding cycle. Electrode type was a truncated RWMA [25] class 2 with 6 mm face diameter. A constant flow of water of 4 L/min at 20 °C was utilised for cooling the electrodes. Welding procedures were carried out according to American Welding Society (AWS) standards [26].

The schematic cross-section of resistance spot welded DP steel in Fig. 2 shows the distribution of different regions which form after welding. The FZ is displayed at the far left side and the unaffected BM at the right. The HAZ has been conveniently sub-divided at the location of Ac_1 as: upper-critical HAZ and sub-critical HAZ.

The IIT tests were performed in a Hysitron triboindenter TI-900. The attached Berkovich indenter was calibrated using a standard fused silica specimen. A range of indentation loads between 750 and 6000 μN was utilised in order to obtain varied displacements for the indenter by penetrating the BM surface. Two regions, namely BM and sub-critical HAZ, were evaluated. Nanoindentation trials were conducted by applying a minimum of 10 indentations per assessed phase (i.e. martensite, ferrite, etc.). A loading–unloading cycle of 20 s was set up.
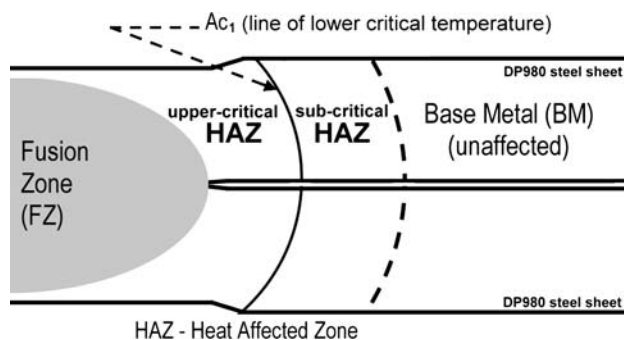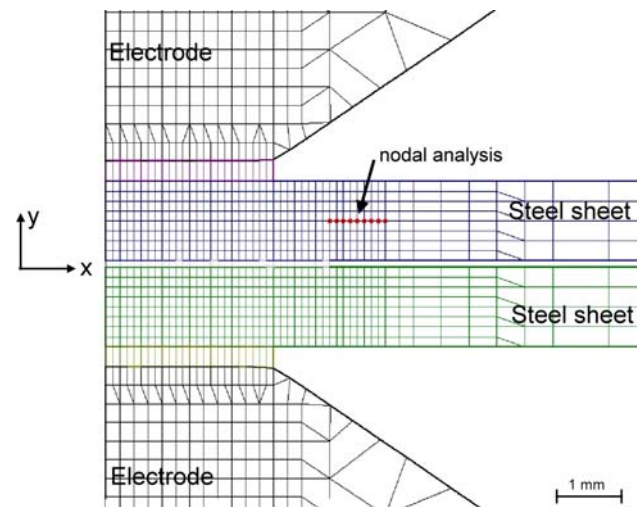
Fig. 3 Two-dimensional axisymmetric model showing the details of meshing for the stacked DP steel sheets

Numerical simulations were conducted in order to obtain an estimate of the peak temperature profile along the subcritical HAZ. Simulations were carried out using commercial finite element software: Quick Spot (by Research Center of Computational Mechanics, Inc., Japan) with coupled electrical–thermal–mechanical analysis [27]. A two-dimensional axisymmetric elastic–plastic model with a total number of 1442 nodes was introduced as depicted by Fig. 3. Mesh density in the HAZ was of 53 elements per mm^2 where nodes were separated from each other by 0.125 mm in "x" direction and 0.15 mm in "y" direction. Material properties (i.e. thermal conductivity, specific heat, thermal expansion coefficient, density, electrical conductivity, Young's modulus and yield strength) for steel having nominal tensile strength of 980 MPa were considered to be temperature dependent. Example of properties at room temperature has been listed in Table 2 [28, 29]. Welding parameters used in these calculations were similar to those established experimentally (i.e. 8 kA, 3.5 kN during 20 cycles). The peak temperature at the sub-critical HAZ was obtained through nodal analysis as detailed by the highlighted points in Fig. 3. Numerical simulations of thermal cycles in RSW of AHSS were conducted as part of previous studies [30, 31] in which cooling rates and microstructure were successfully correlated.

Results

Base metal

IIT trials were conducted upon three different surface conditions (preparation methods) of the BM of DP steel in

Fig. 2 Schematic cross-section of a resistance spot weld

Table 2 Material properties of DP980 at room temperature

Thermal conductivity (W/m/K)	Specific heat (J/(kg K))	Thermal expansion coefficient (1/K)	Density (kg/mm^3)	Electrical conductivity (1/(Ω mm))	Young modulus (GPa)	Yield strength (MPa)
55	458	0.03	7.85E−06	2410	218	600
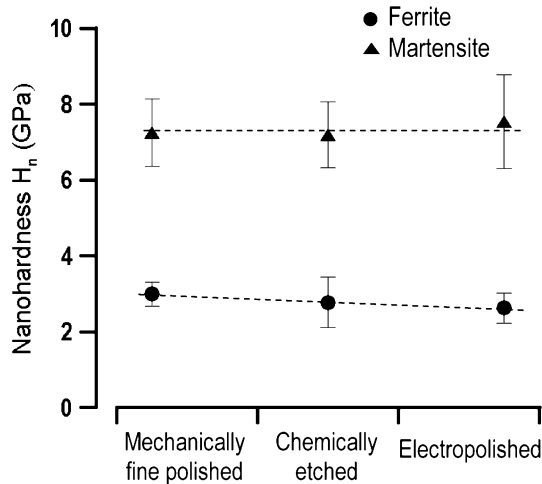
Fig. 4 Effect of surface condition on nanohardness of microstructural phases in BM

Table 3 Roughness parameters for various surface conditions applied to DP steel

Roughness parameter	Roughness (nm)				
	Mechanically fine polished	Chemically etched		Electropolished	
		Ferrite	Martensite	Ferrite	Martensite
R_a	0.9	6.8	21.2	28.5	51.7
R_t	13.0	42.6	72.0	261.5	351.4

order to obtain the most suitable condition for conducting nanoindentation.

Figure 4 shows the average nanohardness (H_n) for ferrite and martensite phases on the mechanically fine polished, the chemically etched and the electropolished surfaces under maximum indentation load (P_{max}) of 3000 μN. Variations in nanohardness were insignificant for martensite between the assessed surface conditions. The dispersion of data for martensite shown by the error bars may be attributed to two main factors: first, due to local variations of supersaturated carbon in the martensitic particles [32, 33]; and second, due to presence of a diverse number of sub-grains (laths) within the martensitic particles [34, 35]. The nanohardness for the ferritic matrix showed slight differences among the three different surface conditions due to possible presence of thin hardened surface layers produced by the mechanical polishing process. Data dispersion for ferrite was lower than for martensite particles; this was probably promoted by a less heterogeneous (free of low and large angle sub-grains) ferritic structure underneath the indenter in contrast to that of martensite (i.e. laths) [36, 37].

Roughness parameters for three different surface conditions obtained under SPM are outlined in Table 3. A relatively lower roughness was found on the mechanically fine polished surface in which R_a laid around 1 nm and R_t around 13 nm. The increased roughness on the etched surface revealed the influence of the chemical attack. A

protrusion effect on martensite particles over the ferrite matrix after etching is observed in Fig. 1. It may be mentioned here that roughness was measured separately on individual ferrite and martensite phase particles. The local roughness (i.e. individual phase) was lower for the ferrite matrix. The electropolished surface resulted in the highest roughness values compared to the other surface conditions. Protrusion effect was hardly present on the electropolished surface due to slight etching of the ferrite matrix. Roughness becomes critical when the surface topography is nonnegligible compared to the maximum indentation depth [38, 39]. Even though it can be inferred that an electropolished surface is free of any hardened layers, the roughness in this case is relatively higher in comparison to the other surface conditions which might influence the indentation process. Roughness for the mechanically fine polished followed by etching procedure was reasonable for nanoindentation measurements in which the range of displacements of the indenter was around 50–250 nm; additionally, this surface condition further reduced possible hardened layers produced by preliminary fine mechanical polishing procedures. Based on above-mentioned observations, mechanically fine polished surface followed by etching was adopted for the remainder of the work carried out in the present study.

The effect of indentation load, in terms of contact depth, on the nanohardness for martensite and ferrite phases is illustrated in Fig. 5. A range of P_{max} from 750 to 6000 μN was used and the nanohardness was plotted as a function of the contact depth (h_c). The nanohardness appeared almost constant on the ferrite matrix for h_c above 150 nm; however, for smaller contact depths (i.e. 100 nm and less) the indentation size effect (ISE) [40, 41] was evident and the measured nanohardness for ferrite increased while h_c decreased. A fluctuation in the average nanohardness for martensite was found (i.e. 7.2–8.2 GPa) for the assessed
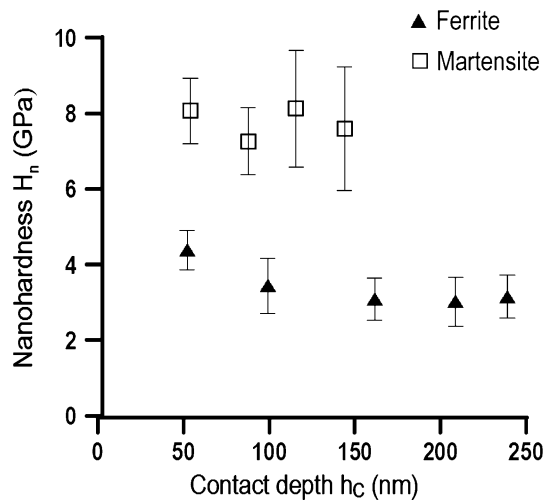
Fig. 5 Effect of indentation load in terms of contact depth on the nanohardness of DP steel

range of contact depths. ISE was not observed for the martensite phase. Nanohardness trials were conducted using an indentation load of 3000 μN (i.e. 161 nm for BM-ferrite and 87 nm for BM-martensite) for the remainder of this work as this was found appropriate in terms of indentation size (depth–width) [24].

Sub-critical heat affected zone

Figure 6 depicts a resistance spot welded cross-section macrograph of DP980 steel. Several regions were identified after etching such as: FZ, Ac_1 line dividing the HAZ into upper-critical and sub-critical, and the BM at the extreme right of the macrograph. Two grids of a determined number of microhardness indentations were located at the sub-critical HAZ and the BM. The grid of indentations at the sub-critical HAZ was divided into five columns in order for the hardness to be averaged at specific distances from Ac_1. The columns a, b, c, d and e were located at 100, 200, 400,

600 and 800 μm, respectively, from Ac_1 in the direction towards the BM (Fig. 6). The grid of microhardness indentations at the BM was located far enough from Ac_1, as seen at the extreme right of the image.

The SEM micrographs shown in Fig. 7 illustrate the microstructures at the sub-critical HAZ combined with that of the BM. The sub-critical HAZ microstructures were obtained at various distances from Ac_1 on the locations detailed in Fig. 6 (i.e. 100, 200, 400, 800 μm and BM). The microstructure at 100 μm away from Ac_1 (Fig. 7a) shows the ferrite matrix (dark regions) and martensite phase severely decomposed (bright regions), or in other words, TM. It may be noted that TM appears broken with presence of sub-micron particles due to nucleation and growth of carbides as indicated by the white arrow marks [24]. Similar microstructural characteristics were observed at 200 μm far from Ac_1 (Fig. 7b). However, here the grain or phase boundary between ferrite and TM appeared sparsely wiped in comparison to that of Fig. 7a, possibly due to a lower volume fraction of carbide precipitation at or near the grain phase boundaries (white arrow) [42]. Figure 7c depicts the microstructure at 400 μm far from Ac_1 in which prior martensitic grain boundaries were clearly defined; basically finer sub-micron particles were observed within martensite grains (white arrow) in contrast to those found in Fig. 7a. An apparent lower volume fraction of fine sub-micron particles were observed in the microstructure obtained at 600 μm far from Ac_1 (Fig. 7d). Figure 7e shows the microstructure at 800 μm far from Ac_1; sub-micron particles were barely visible, however, the martensite did have a decomposed appearance, compared to the original BM microstructure (Fig. 7f) where solid martensitic particle morphology was observed. A general trend revealed that sub-micron particles for TM became finer and a reduction of the volume fraction was also evident as the distance from Ac_1 towards the BM increased. This trend was basically promoted by the welding thermal cycles and the peak temperature profile along the sub-critical region.

Fig. 6 Cross-section macrograph of resistance spot welded DP steel showing two grids of microhardness indentations (HV-200 g) on the sub-critical HAZ (*left*) and BM (*right*). Distance between Ac_1 and the columns of indentations averaged: *a* 100 μm, *b* 200 μm, *c* 400 μm, *d* 600 μm and *e* 800 μm
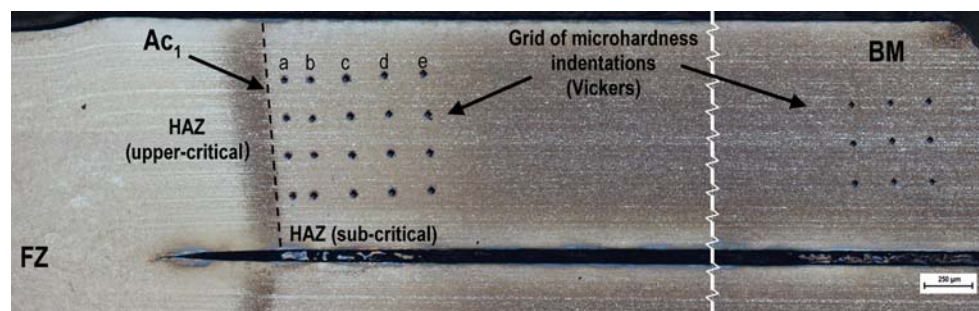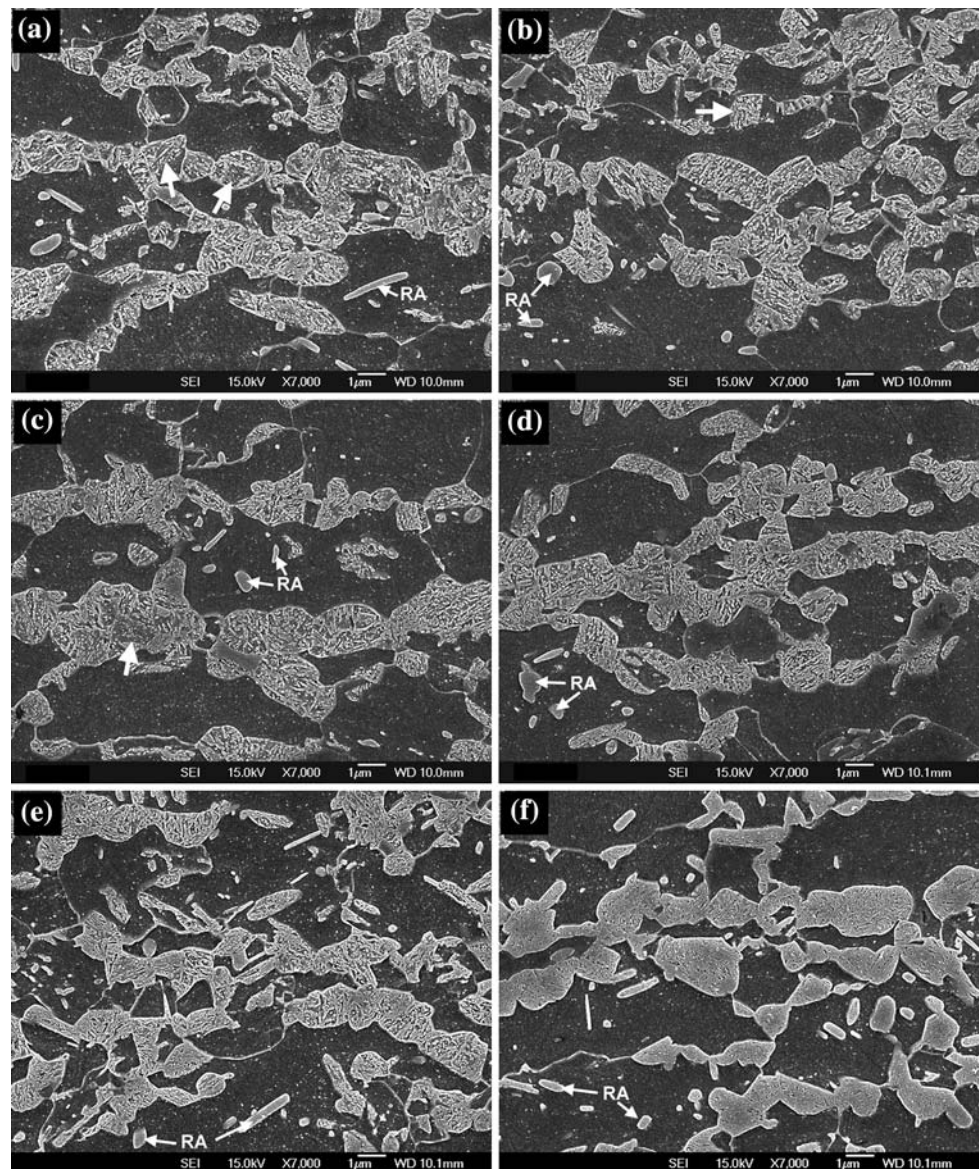
Fig. 7 Sub-critical HAZ microstructures obtained at a distance of: **a** 100 μm, **b** 200 μm, **c** 400 μm, **d** 600 μm, **e** 800 μm from Ac_1 line. **f** Base metal micrograph showing ferrite matrix (*dark regions*) and martensite particles (*brighter regions*)

Low volume fraction of possible retained austenite was consistently found in all of the above-mentioned locations as pointed by the arrow with the label RA in Fig. 7. Presence of retained austenite in the BM was due to the relative high Mn content in the alloy (Table 1) that served as austenite-stabiliser [43]. Similar observations regarding to presence of retained austenite have been reported on welded low alloyed steel when the material was reheated [44].

The average Vickers microhardness (HV) at various distances from Ac_1 towards the BM is shown in Fig. 8. The average microhardness for BM was approximately 301 ± 9 HV. An average softening of about 31 HV was obtained at 100 μm with respect to the centre of the indentation mark. A gradual increase of microhardness was observed as the distance from Ac_1 increased (i.e. at 200,

400 and 600 μm). The average microhardness at 800 μm was of 301 ± 6 HV; thus matching with the microhardness of the BM.

Figure 9 shows the average nanohardness (H_n) of BM-martensite, TM and that of the ferrite matrix obtained at various distances from Ac_1. Slight reduction in nanohardness was observed in ferrite near the location of Ac_1. Insignificant variation of H_n was observed in ferrite at 200 μm and farther distances away towards the BM. Martensite in the BM averaged a nanohardness of 7.2 ± 0.8 GPa. In contrast, nanohardness of TM at 100 μm away from Ac_1 revealed a reduction in hardness (4 ± 1.2 GPa) and approximately similar value was found at 200 μm from Ac_1. A gradual increase in nanohardness was encountered at 400 μm and above for TM until it reached the nanohardness value for martensite in the BM.
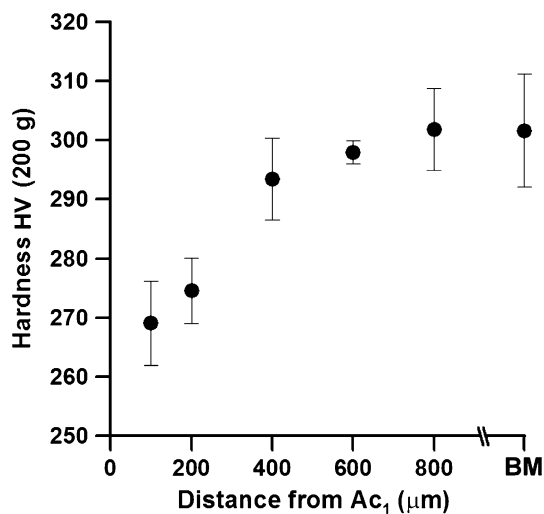
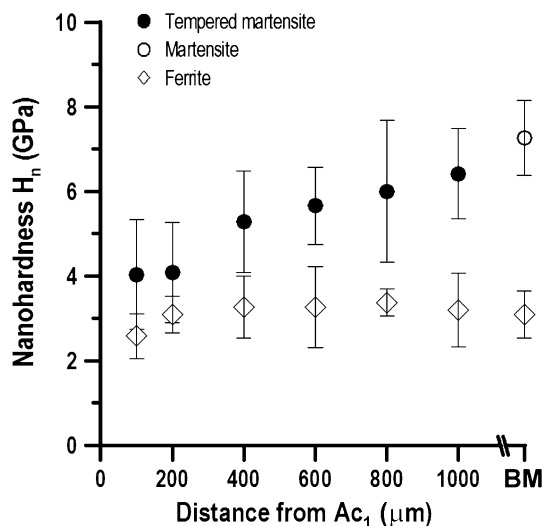Fig. 8 Vickers microhardness at various distances from Ac_1

Fig. 9 Variation of nanohardness (Berkovich) of martensite, tempered martensite and ferrite phase with distance from Ac_1

Fig. 10 P–h curves for base metal (BM) and tempered martensite (TM) at 100, 800 and 1000 μm from Ac_1

indentation (i.e. contribution of high-angle grain boundaries), in contrast, nanoindentation provided an improved resolution in measuring softening due the possibility of avoiding the contribution of the phase boundaries (i.e. TM at low temperature and ferrite boundary) in DP steel.

Figure 10 illustrates the nanoindentation load–displacement (P–h) curves for the BM-martensite and TM at 100 μm (TM_{100}), 800 μm (TM_{800}) and 1000 μm (TM_{1000}) from Ac_1. The BM-martensite resulted in the lowest displacement and hence was confirmed to be the hardest phase. The TM_{100} displayed the largest displacement of all the curves confirming that TM at this location had the lowest hardness (Fig. 9). Continuous deformation without pop-in was commonly found during the loading stage for all the assessed curves [24]. Instead the P–h curve for TM_{100} showed slight discontinuities which might be attributed to the severity of tempering at this location.

Discussion

Tempering of martensite is dependent on time and temperature of thermal exposure. For transient thermal exposures of similar shape but different peak temperature, the extent of tempering will vary according to the maximum temperature attained by the material [17]. During RSW, a gradient of peak temperature will be seen at varying distances from the FZ [45]. However, it is difficult to obtain the peak temperature distribution experimentally for resistance spot weldments due to the presence of strong magnetic fields generated during the welding process. Hence, a numerical simulation was developed in the present work in order to estimate the peak temperature gradient along the sub-critical HAZ. Figure 11 provides a

According to the results plotted in Fig. 8, the average BM microhardness was measured at a distance of 800 μm respect to Ac_1, while at the same location (i.e. 800 μm) and according to the data from Fig. 9; the nanohardness value was well below that of martensite in the BM. The reduced nanohardness at this location was presumed to be due to early stages of tempering (i.e. tempering at low temperature). The characteristics of tempering at low temperatures are discussed in more detail further on. The observed microstructure at 800 μm from Ac_1 (Fig. 7e) contained prior martensite particles still having a tempered appearance with barely visible submicron particles. The fact that microhardness testing was not able to measure softening at 800 μm from Ac_1; might be attributed to a possible grain boundary effect that was promoted by the size of the
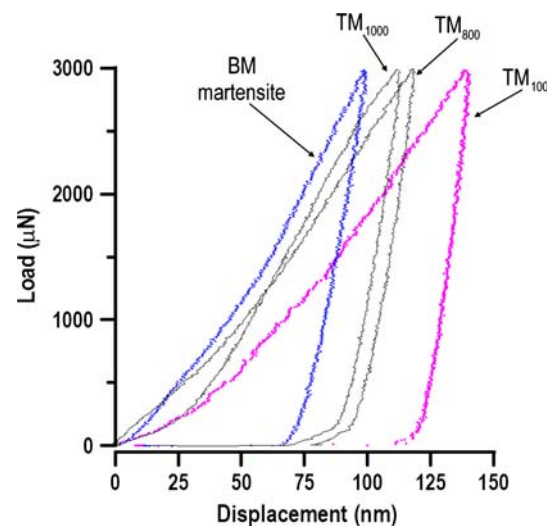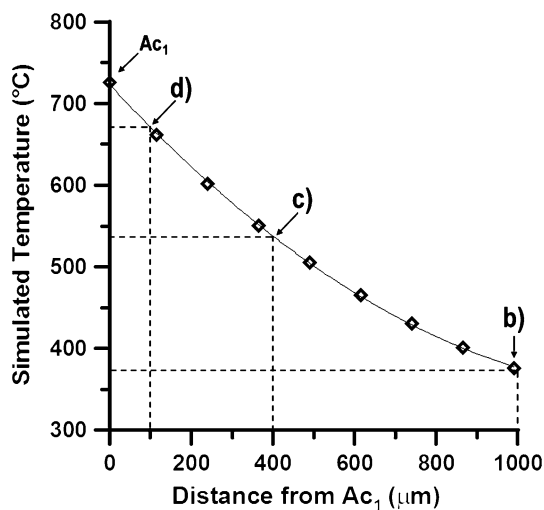
Fig. 11 Numerical simulation of peak temperature at various distances from Ac_1

reference for the temperature distribution along the sub-critical HAZ in DP980 in which numerically simulated peak temperatures were plotted versus the distance from Ac_1 (in the plot, Ac_1 temperature is located at the origin of x-axis). The BM-martensite microstructure in Fig. 12a depicted a solid morphology of untempered martensitic grains. The detailed microstructures from three different locations (labelled as b, c and d in Fig. 11) on the sub-critical HAZ are illustrated in Fig. 12b–d.

Tempering at low temperatures involves several reactions that often overlap and occur in a very fine scale. For instance, the transition carbides (i.e. ε-iron) transform to form cementite in the temperature range of 250–500 °C [18]. Addition of Mn actually retards the coalescence and growth of carbides (finer appearance); thus retaining the morphology of the prior martensitic microstructure [16]. In the temperature range between 350 and 600 °C the original martensite laths remain almost stable with considerable rearranging of dislocations [35]. However, it should be noticed that these statements refer to tempering under isothermal conditions. Figure 12b recorded at a distance of 1000 μm from Ac_1, which attained a temperature of 376 °C as suggested by Fig. 11, revealed more of the solid prior martensite regions predominantly in the outer periphery, but with presence of slightly broken appearance mainly towards the centre of the grain. Figure 11 indicated that a peak temperature of 538 °C was achieved at a distance of 400 μm from Ac_1. Figure 12c shows the tempered martensitic regions observed at this location in which presence of sub-micron particles along with clearly delineated phase boundary between the ferrite and TM regions were clearly observed.

At relatively higher tempering temperatures several other reactions might also occur. Formation of stable
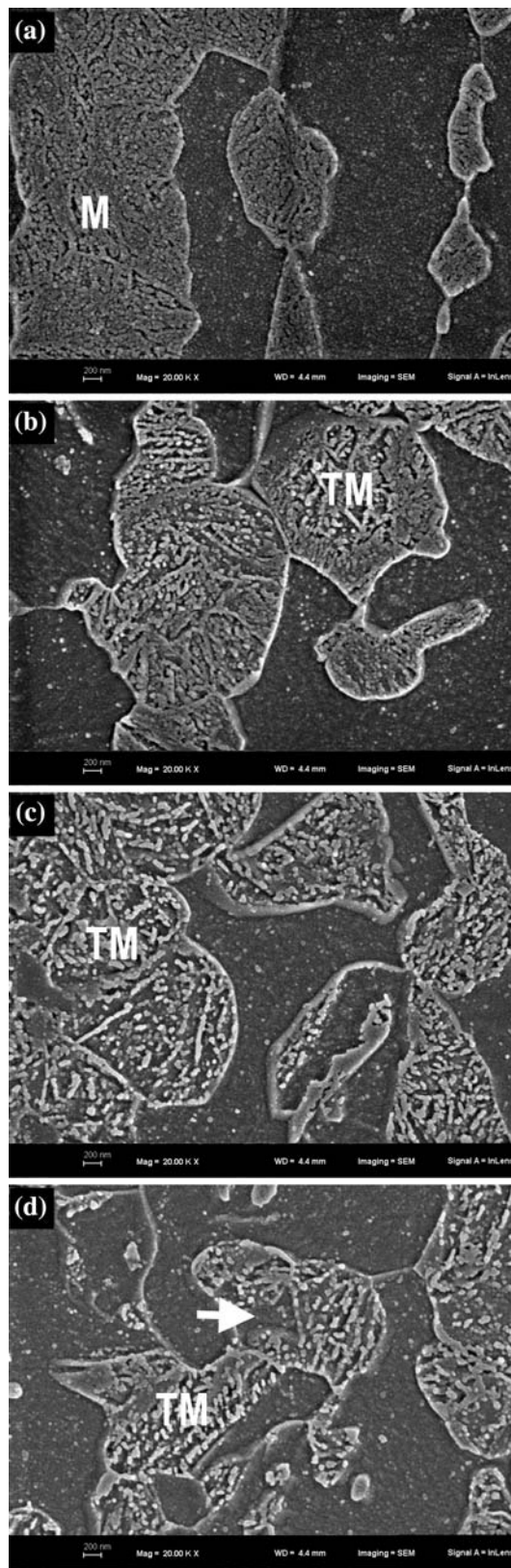
Fig. 12 SEM micrographs illustrating the microstructure of: **a** the BM-martensite (M), and the tempered martensite (TM) regions observed at **b** 1000 μm, **c** 400 μm and **d** 100 μm, far from Ac_1

carbides from alloyed martensites takes place in the range of temperatures between 450 and 700 °C in which dissolution of cementite is also observed [18]. Additionally, considerable spheroidization of carbides above 600 °C has been reported for DP steel containing relatively high Mn content [46]. Recovery or recrystallization is an important reaction that occurs during the tempering process in the temperature range 600–700 °C [47]. Again the above-mentioned observations were achieved under isothermal heat treatment conditions. From Fig. 11 it is seen that a peak temperature of 671 °C was reached at 100 μm far from Ac_1. The TM region shown in Fig. 12d (corresponding to a location 100 μm from Ac_1) depicts a broken appearance containing a large number of spherical submicron particles (presumably carbides) which are abundant near to phase boundaries. The broken morphology along with localised wiped regions (marked by arrow) within the prior martensitic regions suggests partial recovery of martensite. Thus, it is concluded that partial decomposition of martensite has occurred in the sub-critical HAZ assisted by the rapid thermal cycles (fast heating and cooling) developed in the resistance welding process.

Even though an exhaustive SEM analysis of the surface morphology of TM was done at various distances far from Ac_1, still more detailed analysis through transmission electron microscopy is needed in order to fully confirm carbide precipitation and/or recovery of martensite, which was beyond the scope of this paper. The further work is being carried out to confirm the carbide precipitation in the TM regions (Baltazar Hernandez VH, Zhou Y, Unpublished results).

Maximum softening resulted at 100 μm from Ac_1 in which it was properly measured at two levels: nano and micro (Figs. 8, 9). The hardness "jump-up" revealed at 400 μm was more evident on microhardness results; due to the fact that it was strongly influenced by a phase boundary effect. At the location 1000 μm away from Ac_1, the instrumented nanoindentation hardness technique was capable of revealing softening on tempered particles.

The nanoindentation results appeared strongly consistent with the microstructures and the simulated peak temperatures; thus providing a better solution and way for assessing softening of or tempering at low temperatures achieved in RSW process.

Conclusions

1. Several surface preparation procedures were assessed for evaluating the hardness at nano-level. Combination of fine mechanical polishing followed by etching was revealed to produce an acceptable surface condition for assessing BM and HAZ of resistance spot welded dual phase steel through instrumented hardness nanoindentation.

2. The "actual" extension of HAZ-softening was satisfactorily explored through nanoindentation hardness by evaluating TM regions at various distances from the line of lower critical temperature Ac_1. Nanoindentation seems to provide better resolution for assessing softening especially at low temperatures far from Ac_1.

3. The degree or severity of martensite tempering evaluated through instrumented nanoindentation techniques resulted in good agreement with the observed microstructures and with the simulated temperature profile along the sub-critical HAZ.

References

1. Committee on Automotive Applications (2006) In: International Iron and Steel Institute (eds.), Advanced High Strength Steel (AHSS) Application Guidelines Version 3, pp 1–4
2. Tumuluru MD (2006) AWS sheet metal welding conference XII, Livonia, MI, paper 7–5
3. Marya M, Wang K, Hector LG, Gayden X (2006) J Manuf Sci Eng 128:287
4. Ghosh PK, Gupta PC, Avtar R, Jha BK (1990) ISIJ Int 30(3):233
5. Baltazar Hernandez VH, Kuntz ML, Khan MI, Zhou Y (2008) Sci Technol Weld Join 13(8):769
6. Khan MI, Kuntz ML, Zhou Y (2008) Sci Technol Weld Join 13(1):49
7. Panda SK, Sreenivasan N, Kuntz ML, Zhou Y (2008) J Eng Mater Technol 130:041003
8. Xia M, Biro E, Tian Z, Zhou Y (2008) ISIJ Int 48(6):809
9. Migiakis K, Papadimitriou GD (2009) J Mater Sci 44:6372. doi:10.1007/s10853-009-3878-9
10. Raj B, Saroja S, Laha K, Karthikeyan T, Vijayalakshmi M, Bhanu Sankara Rao K (2009) J Mater Sci 44:2239. doi:10.1007/s10853-008-3199-4
11. Tong W, Tao H, Jiang X, Zhang N, Marya MP, Hector LG, Gayden XQ (2005) Metall Mater Trans A 36A:2651
12. Khan MI, Kuntz ML, Biro E, Zhou Y (2008) Mater Trans JIM 49(7):1629
13. Ma C, Chen DL, Bhole SD, Boundreau G, Lee A, Biro E (2008) Mater Sci Eng A 485:334
14. Mililitsky M, Pakalnins E, Jiang C, Thompson AK (2003) SAE International, World Congress Detroit Michigan, paper 2003-01-0520
15. Krauss G (1990) Steels, heat treatment and processing principles. ASM International, Materials Park, OH
16. Grange RA, Hribal CR, Porter LF (1977) Metall Mater Trans A 8A:1775

17. Venugopalan D, Kirkaldy JS (1977) Hardenability concepts with applications to steel. In: Proceedings of a symposium held at Chicago, pp 249–272
18. Morra PV, Böttger AJ, Mittemeijer EJ (2001) J Therm Anal Calorim 64:905
19. Jennett NM, Pharr GM, McHargue CJ (2006) Philos Mag 86(33–35):5153
20. Oliver WC, Pharr GM (1992) J Mater Res 7(6):1564
21. Ghosh S, Pal TK, Mukherjee S, Das G, Ghosh S (2008) J Mater Sci 43:5474. doi:10.1007/s10853-008-2840-6
22. Hirukawa H, Matsuoka S, Miyahara K, Furuya Y (2003) Mater Lett 58:321
23. Ohmura T, Hara T, Tsuzaki K (2004) J Mater Res 19(1):79
24. Baltazar Hernandez VH, Panda SK, Kuntz ML, Zhou Y (2010) Mater Lett 64:207
25. Resistance Welding Manufacturing Alliance (RWMA) (2003) Resistance welding manual, 4th edn. RWMA, Philadelphia, PA
26. ANSI/AWS/SAE/D8.9–97 (1997) Recommended practices for test methods for evaluating the resistance spot welding behavior of automotive steels. American Welding Society (AWS), USA
27. http://www.rccm.co.jp/seihin/quickspot/index.html. Accessed 21 Jul 2009
28. SORPAS® 8.0 (2007) Swantec Software and Engineering APS
29. Okita Y (2008) Experimental measurements. JFE Steel Corporation, Internal Communications, Chiba, Japan
30. Khan I, Kuntz ML, Chan K, Scotchmer N, Zhou Y (2007) SAE International, World Congress Detroit Michigan, paper 2007-01-1370
31. Baltazar Hernandez VH, Kuntz ML, Zhou Y (2008) AWS sheet metal welding conference XIII, Livonia, MI, paper 1–3
32. Garcia-Junceda A, Caballero FG, Capdevila C, de Garcia Andrés C (2007) Scr Mater 57:89
33. Ohmura T, Tsuzaki K, Matsuoka S (2001) Scr Mater 45:889
34. Furuhara T, Kobayashi K, Maki T (2004) ISIJ Int 44(11):1937
35. Honeycombe RWK, Bhadeshia HKDH (1995) Steels microstructure and properties, 2nd edn. Arnold, Great Britain
36. Lei TC, Lin GY, Cui YX (1994) Fatigue Fract Eng Mater Struct 17(4):451
37. Podder AS, Bhattacharjee D, Ray RK (2007) ISIJ Int 47(7):1058
38. Fisher-Cripps AC (2004) Nanoindentation, 2nd edn. Springer, New York
39. Kim JY, Lee JJ, Lee YH, Jang J, Kwon D (2006) J Mater Res 21(12):2975
40. Nix WD, Gao H (1998) J Mech Phys Solids 46(3):411
41. Ma D, Wo Ong C, Wong SF (2005) J Mater Sci 40:2685. doi:10.1007/s10853-005-2106-5
42. Thomson RC, Miller MK (1998) Acta Mater 46(6):2203
43. Sathiya P, Aravindan S, Soundararajan R, Noorul Haq A (2009) J Mater Sci 44:114. doi:10.1007/s10853-008-3098-8
44. Avazkonandeh-Gharavol MH, Haddad-Sabzevar M, Haerian A (2009) J Mater Sci 44:186. doi:10.1007/s10853-008-3103-2
45. Zhang H, Senkara J (2006) Resistance welding fundamentals and applications. Taylor and Francis Group, Boca Raton, FL
46. Speich GR, Leslie WC (1972) Metall Trans 3:1043
47. Joarder A, Jha JN, Ojha SN, Sarma DS (1990) Mater Charact 25:199